Electrical Power and Energy Systems 141 (2022) 108226

Contents lists available at ScienceDirect

International Journal of Electrical Power and Energy Systems

journal homepage: www.elsevier.com/locate/ijepes

Magnetic and electric antennas calibration for partial discharge charge estimation in gas-insulated substations

Christian Mier [a,*], Armando Rodrigo Mor [b], Luis Castro [a], Peter Vaessen [a]

[a] Delft University of Technology, Mekelweg 4, 2628 CD Delft, the Netherlands
[b] Universitat Politècnica de València, Instituto de Tecnología Eléctrica, Camino de Vera s/n, 46022 València, Spain

ARTICLE INFO

Keywords:
Partial discharges
Calibration
PD sensors
Gas-insulated substations
Charge

ABSTRACT

There are no accepted procedures that quantify the apparent charge of partial discharge (PD) in gas-insulated substations (GIS). This paper proposes a calibration method for PD charge estimation using unconventional electromagnetic sensors: a magnetic loop antenna (inductive coupler) and an electric antenna (capacitive coupler.) The calibration procedure is intended for the voltage double integral method, which is reviewed for magnetic antennas and extended for electric antennas. By injecting low-frequency sinusoidal signals, the calibration constants are determined for two different test setups: the first one being a testbench where the characteristic impedance is matched and the second one a full-scale 420 kV GIS. The calibration method is validated in three ways: with a calibrated pulse in the testbench, a calibrated pulse in a full-scale GIS, and PD defects in the full-scale GIS. The calibration procedure revealed a frequency limit range dependent on the GIS length and the sensor's signal-to-noise ratio. The three validation methods showed low charge estimation errors for the magnetic and electric antennas, demonstrating that the PD calibration method applies to any electric/magnetic detector with a low-frequency derivative response. This research paves the way for better GIS insulation monitoring and PD sensor harmonization.

1. Introduction

An accepted method for insulation diagnosis is partial discharge (PD) measurements, and in many cases, it is a requirement in the acceptance protocol [1]. There are some parameters in the PD that determine the insulation's degradation: repetition rate, PD pattern, and charge magnitude. The last one provides an estimation of the severity of the insulation degradation and harmonizes readings from different sensors: the charge magnitude reading is independent of the sensor characteristics if adequately calibrated and measured. The PD measurements which are performed in accordance with the IEC 60270 [2] are the "conventional methods"; the standard does not provide any recommendation for unconventional instruments, as these methods "do not directly quantify the apparent charge of the PD current pulses." The IEC 60270 is only valid for lumped element devices: big equipment such as cables and gas-insulated substations (GIS) cause significant resonances, attenuations, and reflections in the measurements. On the other hand, [3] demonstrates that unconventional detectors, dealing with conducted signals (not radiated) and for a specific frequency range, can be calibrated, providing charge magnitudes.

The most used unconventional electric method in GIS is the ultra-high-frequency (UHF) sensor; these are capacitive coupled antennas with a bandwidth range of 0.3 GHz to 3 GHz [4]. Reference [5] conclude that it is not possible to estimate the PD charge using the UHF range because of the complex propagation in the transverse electric (TE) and transverse magnetic (TM) mode; additionally, [6] demonstrates that the charge information is found in the PD spectra's low-frequency range. Since UHF sensors' calibration is not possible, CIGRE proposes a guide for sensitivity verification [7]; this procedure establishes the equivalent PD charge sensitivity (of 5 pC) for UHF sensors; however, it does not provide the magnitude (severity) of the PD, unlike a calibration.

A PD sensor that measures solely in the transverse electromagnetic

Abbreviations: PD, partial discharges; GIS, gas-insulated substations; UHF, ultra-high frequency; TE, transverse electric; TM, transverse magnetic; TEM, transverse electromagnetic; V2I, voltage double integral; VNA, vector network analyzer; TF, transfer function; ULF, ultra-low frequency; HFCT, high frequency current transformer.

* Corresponding author.
E-mail address: c.mierescurra@tudelft.nl (C. Mier).

https://doi.org/10.1016/j.ijepes.2022.108226
Received 21 January 2022; Received in revised form 10 March 2022; Accepted 7 April 2022
Available online 13 April 2022

(TEM) mode is, in principle, able to calculate the PD charge. There are several methods for PD charge estimation [6]; however, the voltage double integral (V2I) method is the most suitable for non-flat narrow band sensors [8]. Reference [9] shows a novel GIS PD measuring system consisting of a magnetic loop antenna, and [10] demonstrates that the charge magnitude can be obtained from this sensor using the V2I method. In [11], the magnetic antenna's transfer function (TF) is derived, showing the necessary elements for applying the voltage double integral method. The V2I method for UHF sensors was proposed in other investigations [12], but it was not mathematically and experimentally probed in GIS.

This publication presents the calibration procedure for electric and magnetic antennas. The theory of the V2I method shown in [8] is adopted and demonstrated for capacitive coupled sensors. The calibration method is validated in the testbench presented in [13] and in a full-scale 420 kV GIS, using a calibrator and a test-cell with PD defects. Finally, the calibration and charge estimation methods are presented and evaluated for capacitive and inductive couplers.

2. Electric antenna charge estimation

UHF sensors are capacitive couplers, also known as electric antennas; they are used for frequencies above 300 MHz, making them impossible for charge magnitude estimation. However, the charge measurement is possible if the sensor is used below the TE mode frequency [12]. The UHF sensor was previously represented in [14] as a coupling capacitance between the sensor and the GIS' inner conductor (C_1), in parallel with the sensor's load (R) and parasitic capacitance (C_2) with the GIS enclosure. This model is suitable for low-frequency and when the sensor has a negligible inductance; when the feeder conductor is thin, the inductance (L) of the antenna becomes relevant: Fig. 1 shows an electric circuit diagram which includes the parasitic inductance L. Equations (1) and (2) shows the electric circuit's Kirchoff's Voltage Law equations in the time domain; by solving them in the Laplace domain, (3) shows the transfer function; with V_o being the measured voltage, and V_{pd} the propagated PD voltage.

$$V_{pd}(t) = \frac{1}{C_1}\int_0^\infty i_1(t)dt + \frac{1}{C_2}\int_0^\infty i_1(t)dt - \frac{1}{C_2}\int_0^\infty i_2(t)dt \tag{1}$$

$$\frac{1}{C_2}\int_0^\infty i_1(t)dt = \frac{1}{C_2}\int_0^\infty i_2(t)dt + L\frac{di_2(t)}{dt} + Ri_2(t) \tag{2}$$

$$\frac{V_o}{V_{pd}} = \frac{sRC_1}{s^2LC_2 + s(C_2R + C_1L + RC_1) + 1} \tag{3}$$

Since $C_1 \ll C_2$ ([14]), the previous equation can be simplified as:

$$\frac{V_o}{V_{pd}} \approx \frac{sRC_1}{s^2LC_2 + sC_2R + 1} \tag{4}$$

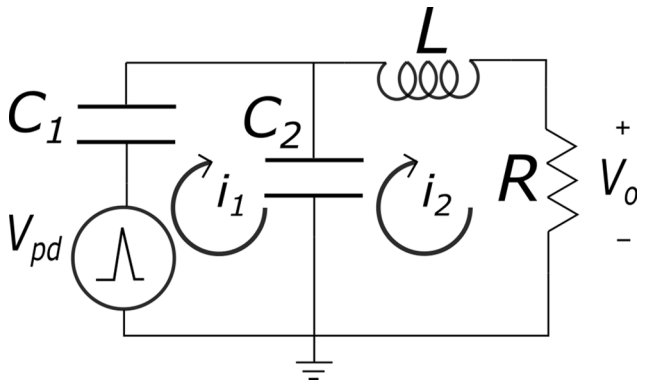

Fig. 1. Electric circuit of an electric antenna.

Equation (4) associates the propagated PD voltage with the measured voltage; to determine the charge magnitude is necessary to know the propagated PD current (I_{pd}). Since the GIS behaves as a transmission line, I_{pd} is obtained with Ohms law (V_{pd}/Z_0), where Z_0 is the characteristic impedance; hence, the output voltage is related to the propagated PD current as shown in (5):

$$\frac{V_o}{V_{pd}/Z_0} = \frac{V_o}{I_{pd}} = H(s) \approx \frac{sRC_1Z_0}{s^2LC_2 + sC_2R + 1} \tag{5}$$

Since the simplified electric antenna's transfer function is a second-order model with one zero at the origin, the theory presented in [8] can be used independently of the sensor's physics; thus, the charge can be estimated using the voltage double integral method:

$$\underbrace{\frac{1}{Z_0}\int_0^t V_{pd}(t)dt}_{q(t)} \approx \frac{LC_2}{RC_1Z_0}V_o(t) + \frac{C_2}{C_1Z_0}\int_0^t V_o(t)dt + \frac{1}{C_1Z_0R}\int_0^t\int_0^t V_o(t)dtdt \tag{6}$$

By evaluating (6) when $t \to \infty$, the first two terms in the right-side hand tend to zero; additionally, [8] demonstrate that the total charge, Q, can be approximated by integrating up to the second zero crossing of the output voltage ($t = t_0$), resulting in (7).

$$Q \approx \frac{1}{C_1Z_0R}\int_0^{t_0}\int_0^{t_0} V_o(t)dtdt \tag{7}$$

The charge evaluation of the magnetic sensor calculated in [10] is shown in (8); in this case, V_o is the measured voltage with the magnetic antenna.

$$Q \approx \frac{1}{M}\int_0^{t_0}\int_0^{t_0} V_o(t)dtdt \tag{8}$$

In both sensors, the coupling element (C_1 or M) is inversely proportional to the charge; additionally, the electric sensor also depends on the resistive load and the characteristic impedance of the PD propagation medium. If there are no GIS discontinuities (change of impedance) close to the sensor's location, the antenna sees a constant voltage-current propagation ratio; therefore, the characteristic impedance is a local phenomenon dependent on the GIS' local geometry and dielectric material ([15]), and the one to be considered for the calibration.

The PD charge estimation using the V2I is proportional to a calibration constant (9). In [8], it is demonstrated that the calibration constant k (M or RC_1Z_0) is approximated to the transfer function at low frequencies. This matches with the slope of the TF in the low-frequency range, representing the sensor's derivative behavior.

$$lim\left|\frac{H(\omega)}{\omega}\right|_{\omega\to 0} \approx k \quad when\ \omega \neq 0 \tag{9}$$

3. Calibration in the testbench

As a first attempt, the calibration constant is obtained experimentally using the testbench presented in [13]. Since the testbench is matched to 50 Ω, it is guaranteed that the injected voltage is the same everywhere in the testbench, including where the sensors are positioned; the matched 50 Ω dictates the ratio between the voltage and current wave. Low-frequency sinusoidal signals were injected and measured in one of the transition cones, and measured at the antenna's output voltage. The sinusoidal signal can be provided by a function generator or a vector network analyzer (VNA) and measured with an oscilloscope or with the same VNA: the VNA results are presented for the testbench and full-scale GIS calibration since it provides a sampled sweep.

Fig. 2 a) and b) (electric and magnetic antenna, respectively) show the measured transfer function $H(f)$ and by using (9), the calculated calibration constant. In the same figure, the slope of the TF is shown: ideally, the calibration frequency range is valid before the slope diverges

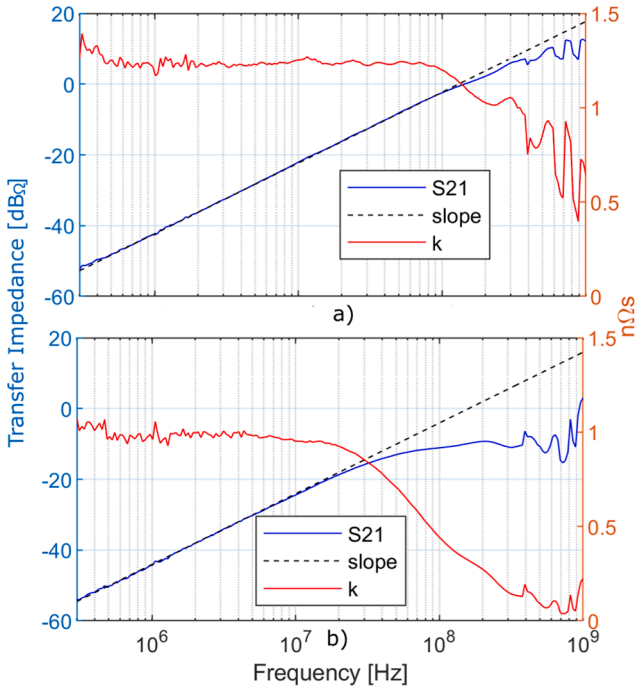

Fig. 2. Electric (a) and magnetic (b) antennas' frequency response, slope, and calibration constant in the testbench [16].

from the TF. At low-frequency, the calibration constant has higher variation; this is caused by the low signal-to-noise ratio of the antenna; at a higher frequency, the constant value starts to decay when the transfer function deviates from the slope. The calibration constant results in 1.22 $n\Omega s$ and 0.95 $n\Omega s$ for the electric and magnetic antenna, respectively.

Given the calibration constants, the charge can be estimated in the testbench. A fast pulse was injected in one of the transition cones using the test setup in [11], and the antenna's output and the reference input were measured (Fig. 3) with a 3 GHz-50 Ω oscilloscope; since the reference pulse was measured with the oscilloscope, the charge was calculated by means of the current pulse integration [6]. Fig. 4 a) shows the reference pulse, and in Fig. 4 b) the measured antennas pulses, using 190 MHz, 8th order low-pass filters, are shown; the electric antenna's oscillating response is originated from the not-flat response and the band-pass filter response behavior of the sensor (bandwidth from tens to hundreds of MHz). The magnetic antenna was measured with a longer cable for better visualization, showing a time delay in Fig. 4 b). Table 1 gives the estimated charges and the error percentage compared to the reference charge; the estimated charge has some error caused by the following reasons: the voltage double integration method is an approximation when the integration time is reduced; and the testbench is not perfectly matched, slightly distorting the propagated pulse.

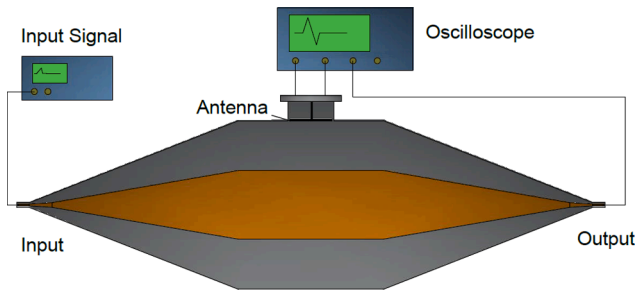

Fig. 3. Testbench used for the pulse charge estimation.

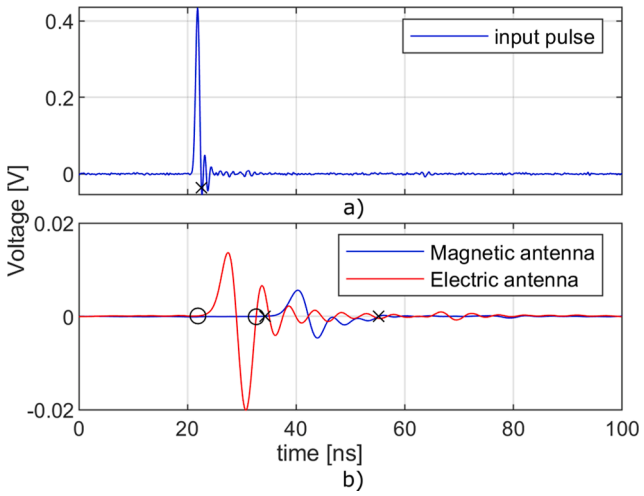

Fig. 4. a) Injected pulse, and b) magnetic and electric antennas' measurement with the corresponding integration time limits (black crosses and circles) [16].

Table 1
Calculated charge and error estimation for the magnetic and electric antenna in the testbench.

	Charge [pC]	Error [%]
Reference	6.9	
Magnetic	6.3	−8.6
Electric	7.3	6.2

4. Calibration in a full-scale GIS

As shown in the previous chapter, the charge calibration constants for both antennas can be evaluated by determining the slope of the transfer function in the derivative response region. The following subchapters explain the setup, results, frequency range limitation, and recommendations for the charge calibration procedure in full-scale GIS.

4.1. Test setup and results

The calibration constant is found either by injecting low-frequency sinusoidal signals with a function generator or a frequency sweep with a VNA; since the full-scale GIS is not matched, a different procedure from the testbench is followed. To calibrate using a VNA is necessary to have access to the output (B) port and reference (R) and test (TA) input ports (Fig. 5 a); this is possible with the Anritzu MS4630B VNA. The magnetic antenna is calibrated in the following way (Fig. 5 b): from the VNA's output port B (or signal function generator), the signal is injected into the GIS; at the GIS input, a high-frequency current transformer (HFCT) is coupled, where its output is connected at the VNA reference port (or oscilloscope); and the antenna's output is connected through an amplifier to the VNA's TA output (or oscilloscope). To relate the antenna's output and the HFCT input current (V_o/I_i), a pre-calibration procedure in the VNA is needed: the output port is connected with a single wire to the test port where the HFCT is coupled, and the HFCT's output is connected to the reference port (Fig. 5 a). The electric antenna is calibrated differently: a sinusoidal signal is injected from the VNA's B output (or function generator) to the GIS in parallel with the VNA's 1 MΩ loaded reference port (or oscilloscope); then the antenna's measured signal goes to the VNA's TA input port (or oscilloscope) through an amplifier; a representation is shown in Fig. 6. A higher calibration sensitivity is obtained by open-circuiting (electric antenna calibration) and short-circuiting (magnetic antenna calibration) the GIS as demonstrated in Fig. 5 b) and Fig. 6.

Fig. 7 shows the frequency response and calibration constant for the

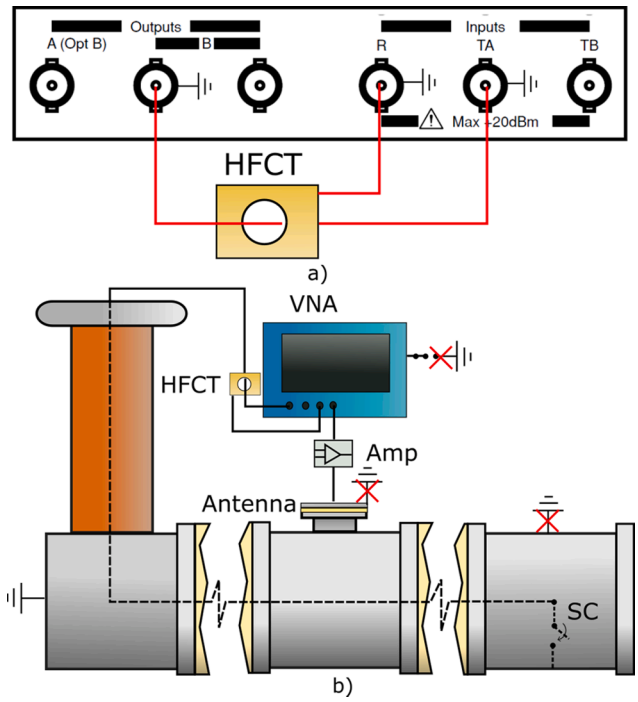

Fig. 5. a) VNA ports and magnetic antenna pre-calibration. b) Magnetic antenna calibration setup in a full-scale GIS.

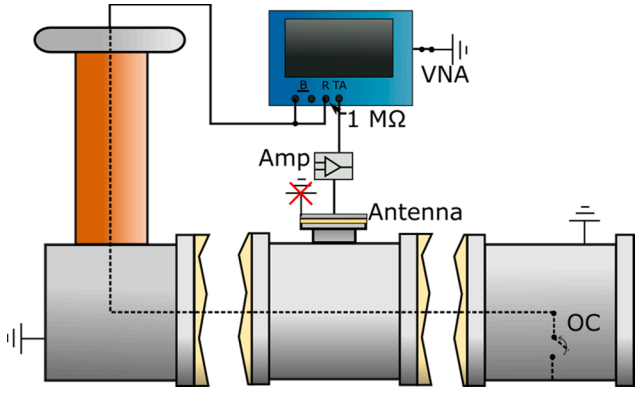

Fig. 6. Electric antenna calibration setup in a full-scale GIS.

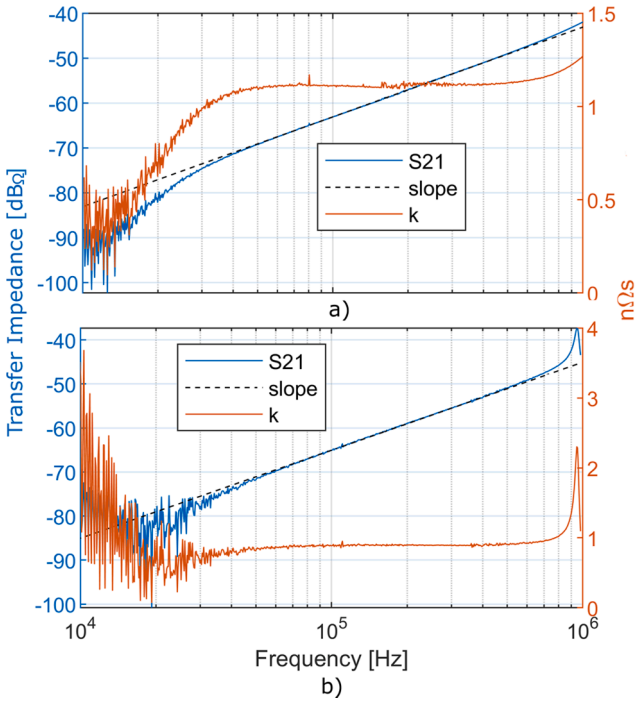

Fig. 7. Frequency response, slope and calibration constant in a full-scale GIS for the a) electric and b) magnetic antennas [16].

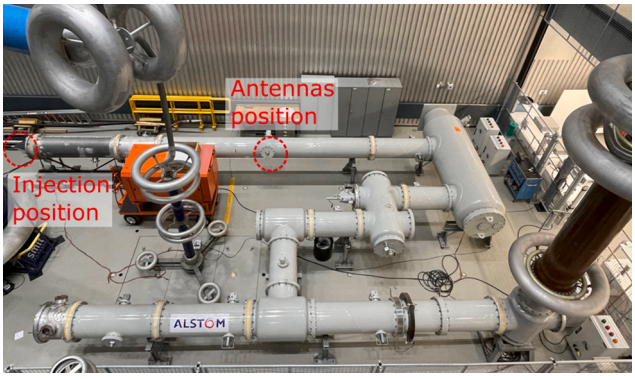

Fig. 8. TUDelft GIS top view indicating the injection point and antennas' position.

electric and magnetic sensors in the TU Delft GIS (Fig. 8). Since the full-scale GIS has a higher interference content, a balance magnetic antenna was used [17]: this antenna has a middle gap in the outer shield, rejecting a higher amount of interference [18]. The magnetic antenna's calibration constant is obtained directly; in the case of the electric antenna, the obtained value must be multiplied by the local characteristic impedance of the GIS. Please note that the calibration is only valid for the specific antenna and the specific location: the transverse geometry of the GIS (inner and outer conductors diameter) and mounting hole dimensions might change for each section. The measurements revealed that although the GIS geometry is different than the testbench, the calibration constants did not change significantly. The calibration constants values for the magnetic and electric antennas are 0.9 nΩs and 1.1 nΩs, respectively (a GIS characteristic impedance of 70 Ω was used); these values were obtained around the frequency of 100 kHz and were used for the next chapters. Fig. 7 shows that the calibration constant can only be obtained a certain frequency range: the reason behind this limitation and the explanation of the deviations for the low and high-frequency range are explained in the following sub-chapters.

4.2. High-frequency limit

The testbench calibration is ideal (it is fully matched): this implies that the voltage (or current) is the same everywhere in the testbench. This is not true for a large GIS if it is not fully matched: reflections modify the voltage (or current) through the GIS. Using TUDelft GIS dimensions ($Z_0 \approx 70\ \Omega$, and a total length$\approx$ 28 m), a simulation (Fig. 9 a) of how the propagated signal changes at the sensor's location relative to the injection point ($V_0/V_i = I_0/I_i = \phi$) was performed. Fig. 9 b) shows how ϕ is affected by frequency and with three different sensor positions relative to the injection point (S): next to the injection point ($S = 1$ m); in the middle of the total GIS length ($S = 14$ m), and in the opposite end of the GIS ($S = 27$ m). Measurements in Fig. 7 show a similar tendency to the simulation when $S = 1$: a resonance is observed near 1 MHz.

Assuming the worst case where the sensor is installed in the opposite side of the injection point ($S = l = 28$ m), the voltage at this position can be obtained using (10): where z is the distance measured from the sensor location; β is the propagation constant, and is equal the angular frequency (ω) over the phase velocity (v_p); and Γ is the reflection

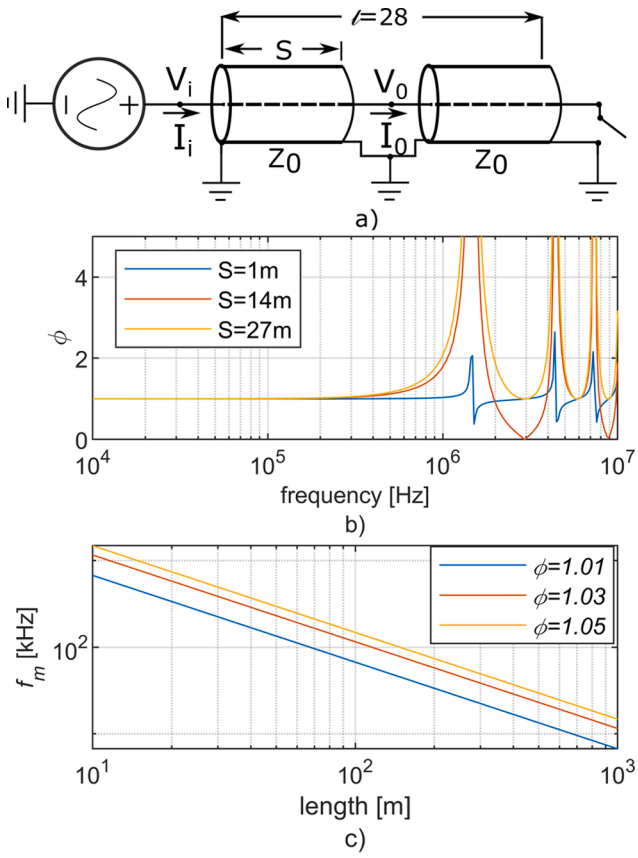

Fig. 9. a) GIS electric circuit representation. b) Signal ratio for different sensor positions. c) Frequency limit as a function of GIS length for 1%, 3%, and 5% of signal variation.

coefficient at the sensor's location.

$$V(z) = V_0^+ \left[e^{-j\beta z} + \Gamma e^{j\beta z}\right] \tag{10}$$

Evaluating (10) when $V(-l) = V_i$ and $V(0) = V_0$ results in (11):

$$\frac{V_0}{V_i} = \phi = \frac{1+\Gamma}{e^{j\beta l} + \Gamma e^{-j\beta l}} \tag{11}$$

By using (11) when the GIS is open-circuited ($\Gamma = 1$), the maximum frequency (f_m), at which the signal variation is equal or less to ϕ, can be obtained as a function of the GIS length resulting in (12). The current ratio (I_0/I_i) evaluation also results in (11) and (12).

$$f_m(l) = -jln\left(\frac{1-\sqrt{1-\phi^2}}{\phi}\right)\frac{v_p}{2\pi l} \tag{12}$$

Using (12), Fig. 9 c) shows the frequency limit for different GIS lengths and signal variations ($\phi = 1.01, 1.03, 1.05$). Previous equations are just an approximation: a real GIS has multiple discontinuities with different characteristic impedances, and the short and open circuits have inductance and capacitance.

4.3. Low-frequency limit

In the low-frequency range, the noise can be attributed to the following reasons (ordered by higher contribution):

- Sensor's sensitivity: the antennas' sensitivity is proportional to the frequency; even with an amplifier, the signal-to-noise ratio is limited for the low-frequency range.
- Common-mode currents: not all the current returns through the GIS' enclosure; a small percentage of current flows as a common-mode current through the antenna's coaxial cable feeder, inducing noise in the measurements. This noise was already observed at the tens of kHz range, eclipsing the calibration constant value.
- Ground paths: the magnetic antenna couples the current in the GIS' enclosure; hence, any current flowing in another path may affect the calibration constant value. The influence of the ground paths in the measurements was relevant at ultra-low-frequency (ULF).

4.4. Recommendations

In practice, because of cost, weight, or equipment availability, it might not be feasible to use instruments with frequency sweep capabilities. In that case, only a single frequency signal might be available, and calibration can be performed using one or multiple single frequency measurements to calculate the slope. To that end, some recommendations are given for a proper calibration frequency selection:

- The GIS length can be shortened by opening a disconnector (electric calibration) or closing a ground switch (magnetic calibration) close to the sensor, increasing the calibration frequency range.
- The frequency limit is increased by injecting the signal near the sensor's location.
- Even though (12) is an approximation, it can be used as a reference for choosing the maximum frequency at which the calibration constant can be obtained. A voltage variation tolerance of 1% is recommended since, as shown in Fig. 9c), the frequency limit increases logarithmically with ϕ but, the calibration constant error increases linearly with ϕ.
- The common-mode current is reduced by insulating the antenna from the GIS (for safety reasons, the antenna must be grounded once it is under operation). The antennas' ungrounding is indicated with a red cross in Fig. 5 b) and Fig. 6.
- If the calibration is performed in the ULF range (<3 kHz), it is recommended that the source and any path that bypasses the magnetic antenna's mounting hole are floated during the calibration process (indicated with red crosses in Fig. 5 b); otherwise, use a higher calibration frequency.

5. Charge calculation with calibrator on a full-scale GIS

Before measuring PD, the calibration method was tested using a calibrated pulse in the GIS. The full-scale GIS cannot be matched with the pulse source, as it was previously done in the testbench: the characteristic impedance of the GIS is not 50 Ω and varies along its length (spacers, circuit breaker, change of geometry, etc.). A transition cone

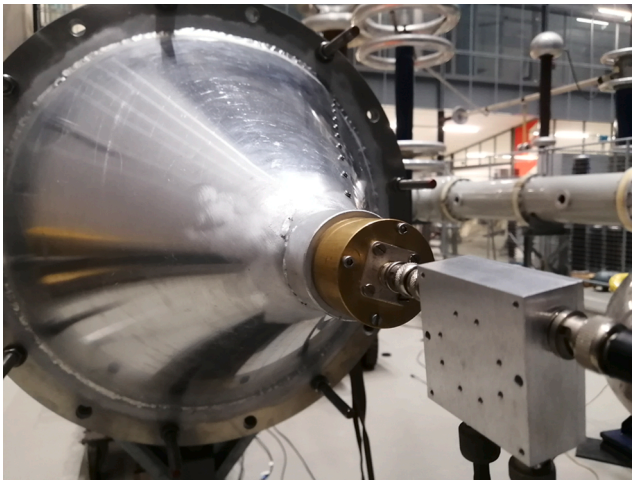

Fig. 10. Picture of the transition cone with the directional coupler.

was used to smooth the transition from the calibrator to the GIS (see Fig. 10): reducing oscillations in the input signal and preventing TEM to TE mode transformation. Since the transition cone and the GIS are not matched with the calibrator's 50 Ω impedance, part of the signal is reflected. A directional coupler was used to measure the transmitted input signal: the transmitted pulse is obtained by subtracting the reflected pulse with the incident pulse.

Fig. 11 a) shows the incident and reflected pulses (at the GIS' injection point) measured with the directional coupler; the reference charge is calculated by subtracting the charge between both pulses: the directional coupler has a broad bandwidth (1–700 MHz), allowing the charge calculation by means of the current pulse integration. Only the first pulse of the reflected signal is used since it represents the transition from the calibrator to the GIS; other reflections result from the GIS discontinuities. Fig. 11 b) shows the magnetic and electric antennas' outputs with 190 MHz 8th order low-pass filters; due to the reflections in the GIS, the measurements show more oscillations than the testbench results. The charge estimations are shown in Table 2; the magnetic antenna showed a lower charge error than the testbench: an overlapped reflection might have contributed to a better charge estimation.

6. Charge calculation with PD on a full-scale GIS

The calibration method is checked with PD test-cells having a jumping particle and surface defect under SF_6 at 3 bars of pressure. Fig. 12 shows the test setup used: the GIS is energized with a HV transformer above the PD inception voltage; the test-cell electrodes are connected to the HV conductor and the ground via a rod and a resistor (attenuating resonances caused by the test-cell); at the grounding rod, a HFCT is coupled to measure the reference pulse; and the antennas' outputs are measured through amplifiers (25 dB 1 GHz voltage amplifier), and filters (190 MHz 8th order low-pass filter); for safety reasons 1 GHz (≈1.5 pF) surge arresters were connected at the oscilloscope input. Since the HFCT has a broad flat gain, the charge can be calculated by means of the current integration.

With the test setup previously explained, 200 PD were measured having the following results: Fig. 13 shows a PD sample in the time domain: a) is the measured HFCT output and b) is the measured antennas' outputs. Fig. 14 shows the comparison between the calculated charges in the antennas (y-axis) and the reference charges (x-axis): for both antennas, the calculated charges are proportional to the reference charge; at a higher magnitude, the electric antenna deviates from the ideal slope, this is associated to the sensor's high gain (at full

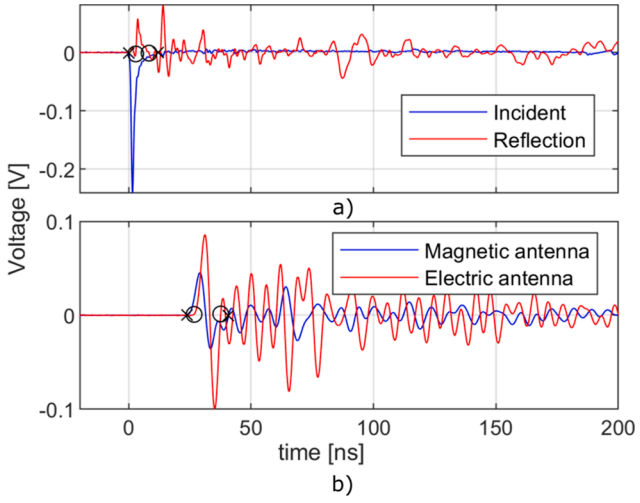

Fig. 11. a) Incident and reflection pulses measured with the directional coupler and b) Magnetic and Electric antennas measurements with their integration time limits (black crosses and circles) [16].

Table 2
Charge and error estimation for the magnetic and electric antenna using a transition cone in a full-scale GIS.

	Charge [pC]	Error [%]
Reference	74.2	
Magnetic	73.3	−1.2
Electric	62.8	−15.4

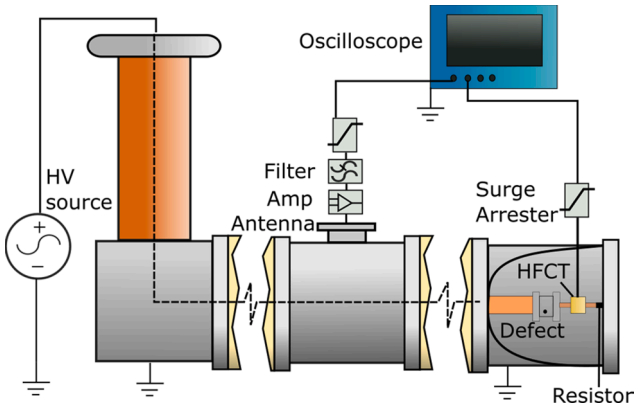

Fig. 12. Test setup for charge estimation in a full-scale GIS.

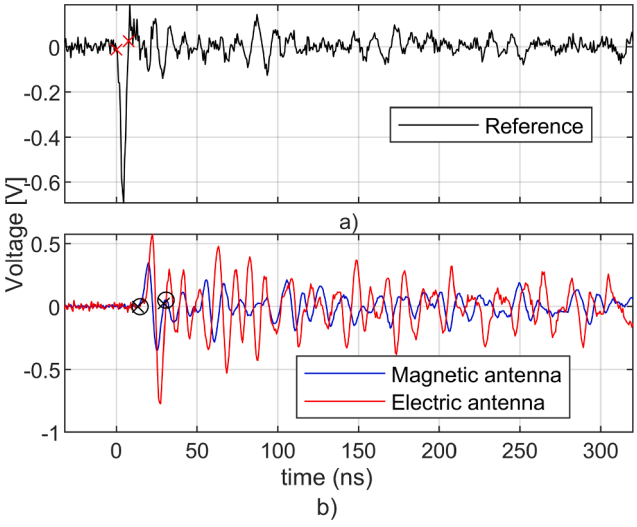

Fig. 13. a) HFCT measured reference pulse and b) Magnetic and Electric antennas measurements with their integration time limits (black crosses and circles) [16].

bandwidth) in combination with the amplifier's non-linearity that distorts the signal Fig. 14 and Fig. 15 show that 78% of the PD measurements performed with the electric sensor have a charge estimation error below 30%, this is attributed to the previous explanation and the Z_0 value approximation. The magnetic antenna shows that 98% of the PD measurements are below 30% error. Both antennas' charge estimation is affected by attenuation and overlapping reflections in the GIS.

Typically, the highest permissible PD in industrial equipment is about 5 pC [19]; hence, any PD measuring system is expected to sense this magnitude. To test the sensitivity of the proposed measuring system, low-magnitude surface PD were measured. Fig. 16 shows the comparison between the calculated charges in the antennas (y-axis) and the reference charges (x-axis); as expected, the charge error is higher than in the jumping particle case; nonetheless, the majority of the PD charges can be evaluated even below 5 pC. By analyzing the waveform of the

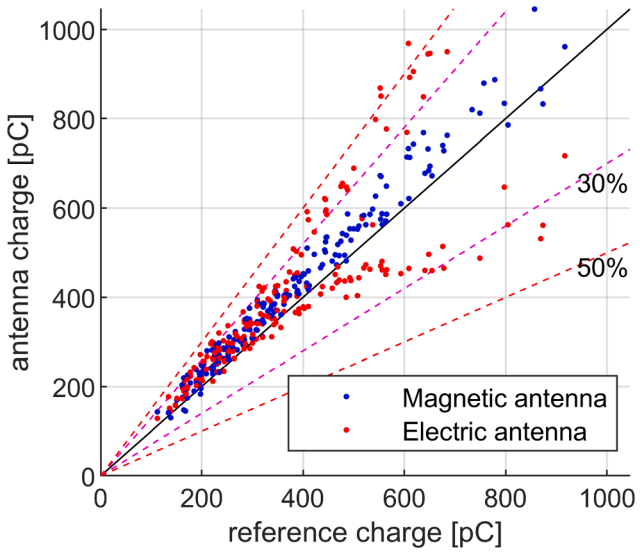

Fig. 14. Antennas and reference charge comparison for 200 jumping particle PD. Dashed lines show 30% and 50% charge estimation error boundaries [16].

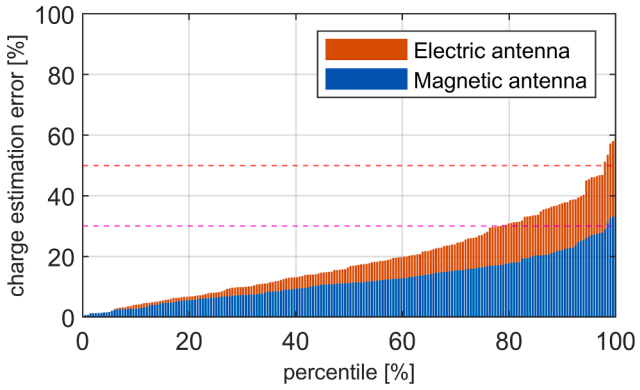

Fig. 15. Charge estimation error percentile. Dashed lines show 30% and 50% charge estimation error boundaries.

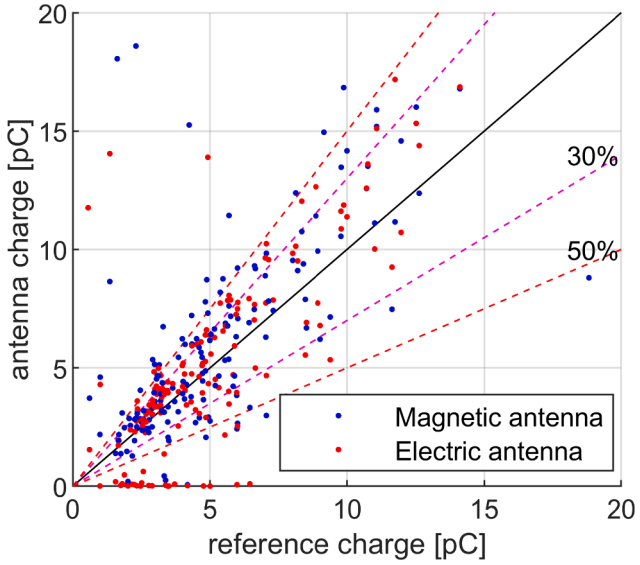

Fig. 16. Antennas and reference charge comparison for surface PD. Dashed lines show 30% and 50% charge estimation error boundaries [16].

most affected charge estimations, it was noted that the error was attributed to low signal-to-noise ratio and interference. The tests were performed in a laboratory where the interference and noise are minimal; further research is needed to simulate an on-site noise environment.

7. Conclusions

The present research proposes a calibration procedure for PD charge estimation using the voltage double integral method. It is shown that the calibration constants can be found in a full-scale GIS by applying sinusoidal signals in the low-medium frequency range (50–500 kHz). The method is extended to derivative electromagnetic sensors, namely magnetic and electric antennas, and experiments showed low charge estimation error for both sensors, confirming the interoperability of the method. The result of this study opens the possibility of measuring PD charge magnitudes with unconventional electric methods, enabling better GIS insulation monitoring and a harmonization value for different sensors. For the next research steps, experiments considering noisy environments (replicating on-site situations) will be performed; and further study to improve the charge estimation accuracy will be carried out, aiming the ± 10% or 1 pC (whatever is bigger) tolerance established in IEC 60270.

CRediT authorship contribution statement

Christian Mier: Conceptualization, Methodology, Formal analysis, Investigation, Writing – original draft, Visualization. **Armando Rodrigo Mor:** Conceptualization, Writing – review & editing, Supervision, Project administration. **Luis Castro:** Methodology, Software. **Peter Vaessen:** Writing – review & editing, Supervision.

Declaration of Competing Interest

The authors declare that they have no known competing financial interests or personal relationships that could have appeared to influence the work reported in this paper.

Acknowledgements

This project 19ENG02 FutureEnergy has received funding from the EMPIR programme co-financed by the Participating States and from the European Union's Horizon 2020 research and innovation programme. Funder ID: 10.13039/100014132.

References

[1] WG D1.33, Guidelines for Unconventional Partial Discharge Measurements, 2010.
[2] IEC 60270, Partial Discharge Measurements, 2015.
[3] Cavallini A, Montanari GC, Tozzi M. PD apparent charge estimation and calibration: a critical review. IEEE Trans Dielectr Electr Insul 2010;17(1):198–205. https://doi.org/10.1109/TDEI.2010.5412018.
[4] Darwish A, Refaat SS, Toliyat HA, Abu-Rub H. On the electromagnetic wave behavior due to partial discharge in gas insulated switchgears: state-of-art review. IEEE Access 2019;7:75822–36. https://doi.org/10.1109/ACCESS.2019.2921089.
[5] Behrmann G, Franz S, Smajic J, Tanasic Z, Christen R. UHF PD signal transmission in GIS: effects of 90° bends and an L-shaped CIGRE step 1 test section. IEEE Trans Dielectr Electr Insul 2019;26(4):1293–300. https://doi.org/10.1109/TDEI.2019.008005.
[6] Mor AR, Morshuis PHF, Smit JJ. Comparison of charge estimation methods in partial discharge cable measurements. IEEE Trans Dielectr Electr Insul 2015;22(2):657–64. https://doi.org/10.1109/TDEI.2015.7076760.
[7] Schichler U, Koltunowicz W, Gautschi D, Girodet A, Hama H, Juhre K, et al. UHF partial discharge detection system for GIS: application guide for sensitivity verification: CIGRE WG D1.25. IEEE Trans Dielectr Electr Insul 2016;23(3):1313–21.
[8] Rodrigo-Mor A, Muñoz FA, Castro-Heredia LC. Principles of charge estimation methods using high-frequency current transformer sensors in partial discharge measurements. Sensors (Switzerland) 20(9);2020. doi: 10.3390/s20092520.
[9] Rodrigo-Morz A, Muñoz FA, Castro-Heredia LC. A novel antenna for partial discharge measurements in GIS based on magnetic field detection. Sensors (Switzerland) 19(4);2019. doi: 10.3390/s19040858.

[10] Rodrigo Mor A, Castro Heredia LC, Muñoz FA. A magnetic loop antenna for partial discharge measurements on GIS. Int J Electr Power Energy Syst 2020;115(June 2019):105514, doi: 10.1016/j.ijepes.2019.105514.
[11] Mier C, Mor AR, Vaessen P. Design and characterization of a magnetic loop antenna for partial discharge measurements in gas insulated substations. IEEE Sens J 2021;21(17):18618–25. https://doi.org/10.1109/JSEN.2021.3089084.
[12] Ohtsuka S, Teshima T, Matsumoto S, Hikita M. Relationship between PD induced electromagnetic wave measured wvith UHF method and charge quantity obtained by PD current waveform in model GIS. Electr Insulat Dielectr Phenomena 2006: 615–8. https://doi.org/10.1109/CEIDP.2006.312007.
[13] Mier C, Mor AR. Test bench and frequency response of a magnetic antenna used in GIS PD measurements 2021;2:269–272, doi: 10.1109/eic49891.2021.9612372.
[14] Kurrer R. Teilentladungsmessung im Gigaherts-Frequencbereich an SF6-isolierten Schaltanlagen. Stuttgart 1997.
[15] Imagawa H, Emoto K, Murase H, Koyama H, Tsuge R, Maruyama S, et al. PD signal propagation characteristics in GIS and its location system by frequency components comparison. IEEE Trans Power Deliv 2001;16(4):564–70.
[16] Mier C. Mag&ElecCalibration. Mendeley Data, V1, 2022. doi: 10.17632/837wftgxzv.1.
[17] Libby LL. Special aspects of balanced shielded loops. Proc IEEE 1946;34(9):641–6.
[18] Carobbi CFM, Millanta LM. Analysis of the common-mode rejection in the measurement and generation of magnetic fields using loop probes. IEEE Trans Instrum Meas 2004;53(2):514–23. https://doi.org/10.1109/TIM.2004.823297.
[19] C. W. 33/23.12. Insulation Co-ordination of GIS: return of experience, on site tests and diagnostic techniques; 1998.